Fluid-structure interaction in phaco-emulsification based cataract surgery

Zhaokun Wang [a,b], Chenglei Wang [a], Fuwang Zhao [a,b], Feng Ren [c], Xiaoyu Luo [d], Hui Tang [a,*]

[a] Department of Mechanical Engineering, The Hong Kong Polytechnic University, Kowloon, Hong Kong, China
[b] School of Fashion and Textiles, The Hong Kong Polytechnic University, Kowloon, Hong Kong, China
[c] School of Marine Science and Technology, Northwestern Polytechnical University, Xi'an, Shanxi, China
[d] School of Mathematics and Statistics, University of Glasgow, Glasgow G12 8QQ, UK

ARTICLE INFO

ABSTRACT

Cataract scatters the light as it enters the eye, blurs images and severely interferes people's daily activities. The only effective therapy is cataract surgery, in which the clouded lens is phacoemulsified and removed. However, an aberrant iris distortion, namely intra-operative floppy iris syndrome (IFIS), is not uncommon in the phaco-emulsification process, and it greatly degrades the surgical outcomes. Despite its great impact, the mechanism of IFIS has seldom been explored from the mechanics viewpoint. This study constitutes the first exploration into IFIS mechanism within the torsional-irrigation/aspiration (T-I/A) combined mode, from the perspective of fluid-structure coupling, employing our newly developed fluid-structure interaction (FSI) simulation framework. The impacts of several factors, including probe type and position, irrigation and aspiration (I/A), iris stiffness and lens presence, are evaluated in two different torsional-irrigation/aspiration (T-I/A) combined configurations, corresponding to the scenarios of coaxial and bimanual I/A operations. Results reveal that by altering the probe's location in anterior chamber, three distinct modes of iris dynamics are recognized and defined as repulsion (RP), attraction (AT), and adhesion (AH) modes according to the relative iris-probe location. Among them, RP mode, where the iris is repelled by the probe, is preferred to ensure the safety of the iris. Furthermore, IFIS could be alleviated by stiffening iris, reducing I/A strength and choosing coaxial I/A device. These interventions result in the contraction of the damaging AH zone towards the iris root, occurring at approximately one-fourth (coaxial case), one-fifth (coaxial case), and one-fourth of the iris length, achieved by quadrupling iris stiffness, ceasing I/A flow, and utilizing coaxial I/A device, respectively. However, the risk of IFIS is only marginally impacted by the lens presence. Our findings gain a deeper insight into the iris dynamics in T-I/A mode from fluid-iris interaction viewpoint, which may provide valuable guidance for the surgical protocol operation.

1. Introduction

Cataract, characterized with a degradation in the optical quality of the crystalline lens, obstructs the light from reaching the retina and impairs clear vision [1–3]. It accounts for more than 33 % of the global visual deterioration and is the leading cause of curable blindness [4]. The circumstance is much more critical in developing nations, e.g., Pakistan having a rate of over 50 % [5]. Given that cataract prevalence increases with age, its incidence is expected to rise as the global population ages [2]. The only effective therapy is phacoemulsification-based cataract surgery, which replaces the cloudy lens with a clear artificial lens [6–8]. Although the surgery is typically successful, intra-operative complications are not uncommon. One of the major risks is abnormal intraoperative iris behavior, known as intraoperative floppy iris syndrome (IFIS), which comprises a triad of signs: intraoperative iris billowing, miosis and a tendency for iris prolapse [9,10]. These aberrant iris movements obstruct the surgeon's vision, prolong the operation time, and thus increase the risk of intraoperative complications, i.e., rupture of the posterior capsule [11,12]. The underlying mechanisms of IFIS, however, are not yet well understood [13]. It is crucial to conduct comprehensive investigations to gain deeper insight into the physical mechanisms underlying IFIS and thereby enhance surgical outcomes.

In general, the mechanics of iris and fluidics in the emulsification process are directly implicated the etiology of IFIS [11,14,15]. Various clinical studies have revealed an association between IFIS and the systemic usage of oral alpha-blockers, i.e., tamsulosin [9,11,16,17]. This medication profoundly alters the mechanical properties of the iris, such as a drop in Young's modulus, which increases the IFIS risk as a side effect [9]. To mitigate the risk of IFIS in these circumstances,

---

Nomenclature

c_α	lattice speed	p^*	nondimensional fluid pressure
c_s	sound speed	Re_I	Reynolds number of I/A mode
EA	iris stretching stiffness	Re_T	Reynolds number of T mode
EA^*	non-dimensional stretching stiffness of iris	s	Lagrangian coordinate along the iris
EI	iris bending stiffness	s^*	non-dimensional Lagrangian coordinate along the iris
EI^*	non-dimensional bending stiffness of iris	S	Relaxation matrix
f^*	non-dimensional frequency	t^*	non-dimensional time
f_e	body force acting on fluid	u	fluid velocity
f_e^*	non-dimensional body force on fluid	u^*	non-dimensional fluid velocity
f_α	particle density distribution function	V_T	amplitude of probe-induced velocity
f_α^{eq}	equilibrium distribution function	V_I	amplitude of irrigation jet velocity
F_f	external fluid loading acting on iris	V_I^*	non-dimensional amplitude of irrigation jet velocity
F_f^*	non-dimensional fluid loading on iris	w_α	LBM lattice weighting
g_α	discrete force distribution function	x	particle position
H_A	aspiration port height	x_p	probe horizontal location
H_A^*	non-dimensional aspiration port height	x_p^*	non-dimensional probe horizontal location
H_f	height of the anterior chamber	x_{pA}	bimanual probe-A horizontal location
H_f^*	non-dimensional height of anterior chamber	x_{pA}^*	non-dimensional bimanual probe-A horizontal location
H_I	irrigation port height	x_{pI}	bimanual probe-I horizontal location
H_I^*	non-dimensional irrigation port height	x_{pI}^*	non-dimensional bimanual probe-I horizontal location
H_p	height of the probe	X	iris position
H_p^*	non-dimensional height of the probe	X^*	non-dimensional iris position
I	identity matrix	y_p	probe vertical location
L	iris length	y_p^*	non-dimensional probe vertical location
L_A	aspiration port length of bimanual probe	y_{pA}	bimanual probe-A vertical location
L_A^*	non-dimensional aspiration port length of bimanual probe	y_{pA}^*	non-dimensional bimanual probe-A vertical location
L_f	length of the anterior chamber	y_{pI}	bimanual probe-I vertical location
L_f^*	non-dimensional length of anterior chamber	y_{pI}^*	non-dimensional bimanual probe-I vertical location
L_I	irrigation port length of bimanual probe	$\bar{y}_{tip}$	mean vertical position of iris tip
L_I^*	non-dimensional irrigation port length of bimanual probe	y_{tip}^*	vertical position of iris tip
L_p	length of the coaxial probe		
L_p^*	non-dimensional length of the coaxial probe	*Greek symbols*	
m^*	non-dimensional mass ratio	ρ_{f0}	mean mass density
M	transformation matrix	ρ_s	line density of the iris
p	fluid pressure	ρ_f	fluid density
		ν	fluid kinematic viscosity

pharmacologic treatment, such as intracameral phenylephrine, is typically utilized as the clinical therapeutic procedure to dilate the pupil, stiffen the floppy iris, and stabilize iris motility, therefore reducing the risk of intra-operative iris injury [9]. Some researchers have conducted studies at elucidating the underlying mechanics of IFIS. Lockington et al. were the first to model IFIS in endothelial graft surgery and describe the mechanism of iris' billowing behavior from the perspective of iris buckling [18]. Their results demonstrate that the iris buckles into a wavy mode under a critical intra-ocular air-bubble-induced pressure. Subsequent research by Qi et al. examined how intraocular phenylephrine influenced the abnormal movement of the iris, and they found that IFIS risk may be lessened by stiffening the iris and dilating the pupil [9]. Lockington et al. further explored the effectiveness of the Malyugin ring (a pupil expansion device) as well as intraocular phenylephrine on inhibiting iris billowing [19].

The fluidics of the emulsification process also exerts a substantial impact on the iris dynamics [20], and the interplay between iris and intense probe-induced flow results in more complex dynamics than those resulting solely from the iris buckling. Several studies have been conducted to investigate the role of I/A flow during phacoemulsification. Yuichi Kaji et al. experimentally visualized irrigation flow in the anterior chamber during phacoemulsification by particle image velocimetry [21]. Abouali et al. carried out the first study to compare bimanual and coaxial I/A techniques and evaluated the fluid dynamics of the I/A flow [22]. Their findings indicated that the coaxial handpiece

with an inner placement of irrigation tip reduced the impact of turbulence on the cornea. Bayatpour et al. extended the research by adopting a numerical model of the cornea to simulate the instability characteristics of anterior chamber from the viewpoint of fluid-structure interaction [23]. They investigated the effects of I/A type on the anterior chamber's instability, and found that the bimanual I/A flow was more likely to trigger instability compared to coaxial I/A flow. Additional studies have been conducted on the FSI of the iris and intraocular flows, which involve various choices, such as whether the iris is linear or nonlinear and whether the fluid is steady or unsteady [24], as outlined in Table 1. However, most of them concentrate on the iris dynamics under aqueous humor flow, where the iris only experiences slight deformation. Iris mechanics in the context of IFIS, when substantial deflection occurs, has not been examined [22,23,25-30]. Recently, we developed a more precise FSI simulation framework to study iris dynamics in the torsional operation (T) mode of the probe, considering both fluid mechanics and the iris' significant deformability [30]. The results demonstrated that IFIS could be mitigated through various means, including increasing the iris stiffness, shortening the iris length (i.e., pupil dilation), decreasing the power of the emulsification probe, and maintaining the probe operation frequency within a proper range. Given the vital role of I/A flow in nucleus removal, it is commonly employed in conjunction with torsional operation, which further increases the complexity of fluid dynamics during surgery. This intensified flow interacts with iris and may induce severe deformation that could

Table 1
Summary of studies on the interaction between the probe-induced flow and iris.

Data source	Flow type	Iris material	Simulation type
Heys et al. [26] (2001)	Aqueous humor flow	Linear elastic	Transient FSI
Heys and Barocas. [27] (2002)	Aqueous humor flow	Linear elastic	Transient FSI
Huang et al. [28] (2004)	Aqueous humor flow	Nonlinear elastic	Steady FSI
Huang et al. [29] (2006)	Aqueous humor flow	Nonlinear elastic	Transient FSI
Amini and Barocas. [25] (2010)	Aqueous humor flow	Nonlinear elastic	Transient FSI
Abouali et al. [22] (2011)	Irrigation and aspiration flow	Excluded	Transient FSI (Flow only)
Takushi et al. [31] (2016)	Aqueous humor flow	Rigid	Transient FSI (Flow only)
Bayatpour, et al. [23] (2017)	Irrigation and aspiration flow	Excluded (cornea studied)	Transient FSI
Wang et al. [32] (2022)	Irrigation and aspiration flow	Excluded	Transient FSI
Wang, et al. [30] (2022)	Torsion-induced flow	Geometrical nonlinear	Transient FSI
Wang, et al. [33] (2023)	Irrigation and aspiration flow	Excluded	Transient FSI

lead to complications if not properly managed. To our best knowledge, still very few studies have been performed on the IFIS mechanism in the I/A-T combined mode from the standpoint of fluid-structure coupling, especially under two distinct coaxial and bimanual I/A scenarios with considering the iris' severe deformation.

In this study, the physical mechanism of IFIS was explored utilizing a two-dimensional configuration in the more realistic scenario of T-I/A combined mode, where both the torsional vibration mode and irrigation/aspiration mode are considered. The effects of key parameters, including probe location, I/A strength, iris stiffness, probe type, and lens presence on surgical outcomes, are investigated in detail. The paper is organized as follows: The problem description, mathematical formulation, numerical method and the verification are described in Section 2. The detailed result regarding IFIS mechanism is discussed thoroughly in Section 3. Finally, some appropriate conclusions as well as clinical guidelines are drawn in Section 4.

2. Problem definition and mathematical formulation

A simplified two-dimensional model is adopted to explore the physical mechanism of IFIS in the T-I/A combined mode, with both the torsional vibration and irrigation/aspiration considered. As depicted in Fig. 1, the eye is modelled as a rectangle of length L_f and height H_f with the coordinate origin O positioned at the center of the model. The iris is represented by two cantilever beams that are arranged opposite to each other and have length L, bending stiffness EI, stretching stiffness EA, and line density ρ_s. The undisturbed beams are placed along the horizontal line $y = 0$, with one end clamped to the side walls at $x=\pm L_f/2$. The aqueous humor is assumed as an incompressible fluid with water-like properties [34]. Two types of handle devices, namely the coaxial and bimanual phacoemulsification probes [22,35], are considered in the present study. The coaxial probe is represented by a rectangular block of length L_p and height H_p, as displayed in Fig. 1(a). The bimanual probes are represented by two separate rectangular blocks, i.e., probe-I (irrigation alone, length L_I and height H_I) and probe-A (coupled aspiration-torsion, length L_A, height H_T), as illustrated in Fig. 1(b). The aspiration is accomplished through continuous suction by applying a zero pressure at the bottom of the probe (denoted by a thick red line), while the irrigation is achieved through a pair of continuous jets issued horizontally with a constant flow rate and a parabolic velocity profile from the two sides of the probe (denoted by blue arrows). The probe's torsional vibration is realized by a pair of oscillatory jets that are

uniformly issued with a horizontal time-varying anti-phase velocity $V = V_T\sin(2\pi t/T)$, where V_T and T are the amplitude and period, respectively (denoted by purple arrows). The filled cyan area at the bottom side denotes the lens.

In this system, the fluid flow is governed by the incompressible Navier–Stokes equations,

$$\nabla\cdot\boldsymbol{u} = 0, \tag{1}$$

$$\frac{\partial\boldsymbol{u}}{\partial t} + \boldsymbol{u}\cdot\nabla\boldsymbol{u} = -\frac{1}{\rho_f}\nabla p + \nu\nabla^2\boldsymbol{u} + \boldsymbol{f}_e, \tag{2}$$

where $\boldsymbol{u}$ is the fluid velocity, ρ_f the fluid density, p the pressure, ν the kinematic viscosity and $\boldsymbol{f}_e$ the external body force term.

The deformation and motion of two flexible filaments are described by the structural equation with large displacement [36,37]

$$\rho_s\frac{\partial^2\boldsymbol{X}}{\partial t^2} = \frac{\partial}{\partial s}\left[EA\left(1 - \left(\frac{\partial\boldsymbol{X}}{\partial s}\cdot\frac{\partial\boldsymbol{X}}{\partial s}\right)^{-1/2}\right)\frac{\partial\boldsymbol{X}}{\partial s} - \frac{\partial}{\partial s}\left(EI\frac{\partial^2\boldsymbol{X}}{\partial s^2}\right)\right] + \boldsymbol{F}_f, \tag{3}$$

where s is the Lagrangian coordinate along the iris, $\boldsymbol{X}$ (x, y) is the position vector of the iris, $\boldsymbol{F}_f$ is the Lagrangian force exerted on the iris by the surrounding fluid and ρ_s is the line density of structure, EI and EA are the structural bending and stretching stiffness, respectively.

Initially, both the fluid and filament are at rest. The clamped boundary condition is applied at the iris ends, which are specified as $X = (\mp 1/2L_f, 0)$, $\partial\boldsymbol{X}/\partial\boldsymbol{s} = (\pm 1, 0)$. The no-slip and no-penetration conditions are enforced on the surfaces of the iris and lens by the immersed boundary method, and the non-reflecting condition is applied on the surrounding walls [38].

The dimensionless parameters and their values are listed in Table 2, which are obtained using the characteristic variables ρ_f, L and V_T. Similar to our previous work [30], the anterior chamber is modelled with a rectangle of length $L_f^* = 3$ and height $H_f^* = 1$. The coaxial probe has a length $L_p^* = 0.3$ and a height $H_p^* = 0.3$ with torsion port height $H_T^* = 0.1$ and irrigation port height $H_I^* = 0.15$. In contrast, the bimanual device has an aspiration port of $H_T^* = 0.1$ on probe-A and an irrigation port of $H_I^* = 0.15$ on probe-I, determined based on the scales of the standard 19-gauge phaco needle [39]. Additionally, for sake of clarity and ease of discussion, the probe-I remains fixed at $x_{pI}^*=0$ and $y_{pI}^*=0.3$ throughout the simulation, unless stated otherwise. The mechanical properties of normal iris are determined from Ref. [9,25], with $EI^* = 0.017$, $EA^* = 24.869$, and $m^* = 0.091$. The torsional vibration characteristics of the probe are assumed to be the same as those in our previous work [30], but with a more realistic Reynolds number $Re=1560$ [25,39,40]. As for irrigation/aspiration, a baseline irrigation intensity of 18 cc/min is employed [39], corresponding to $Re_{IA} = 2294$.

To facilitate this study, the incompressible two-dimensional nine-speed lattice Boltzmann method, denoted as D2Q9 LBM [43], is utilized to solve the fluid dynamics. The multi-relaxation time algorithm(MRT) proposed by Yu et al. (2002) [44] is employed to improve the computational stability. The dynamics of the flexible iris are modeled using the finite-element method (FEM) [45], with the incorporation of a co-rotational scheme to address the geometric nonlinearity [46,47]. The interplay between the elastic iris and its surrounding fluid is dealt with the direct-forcing immersed boundary method [48], integrated into the lattice Boltzmann method to handle the moving boundary and accurately predict the fluid loading on the cantilever. A succinct introduction to the current numerical framework is given in APPENDIX A, accompanied by a convergence study to validate the independence of the current results on the grid and time resolutions.

3. Results and discussion

This section is organized as follows: the iris dynamics with the probe placed at different locations is analyzed at first. Subsequently, we
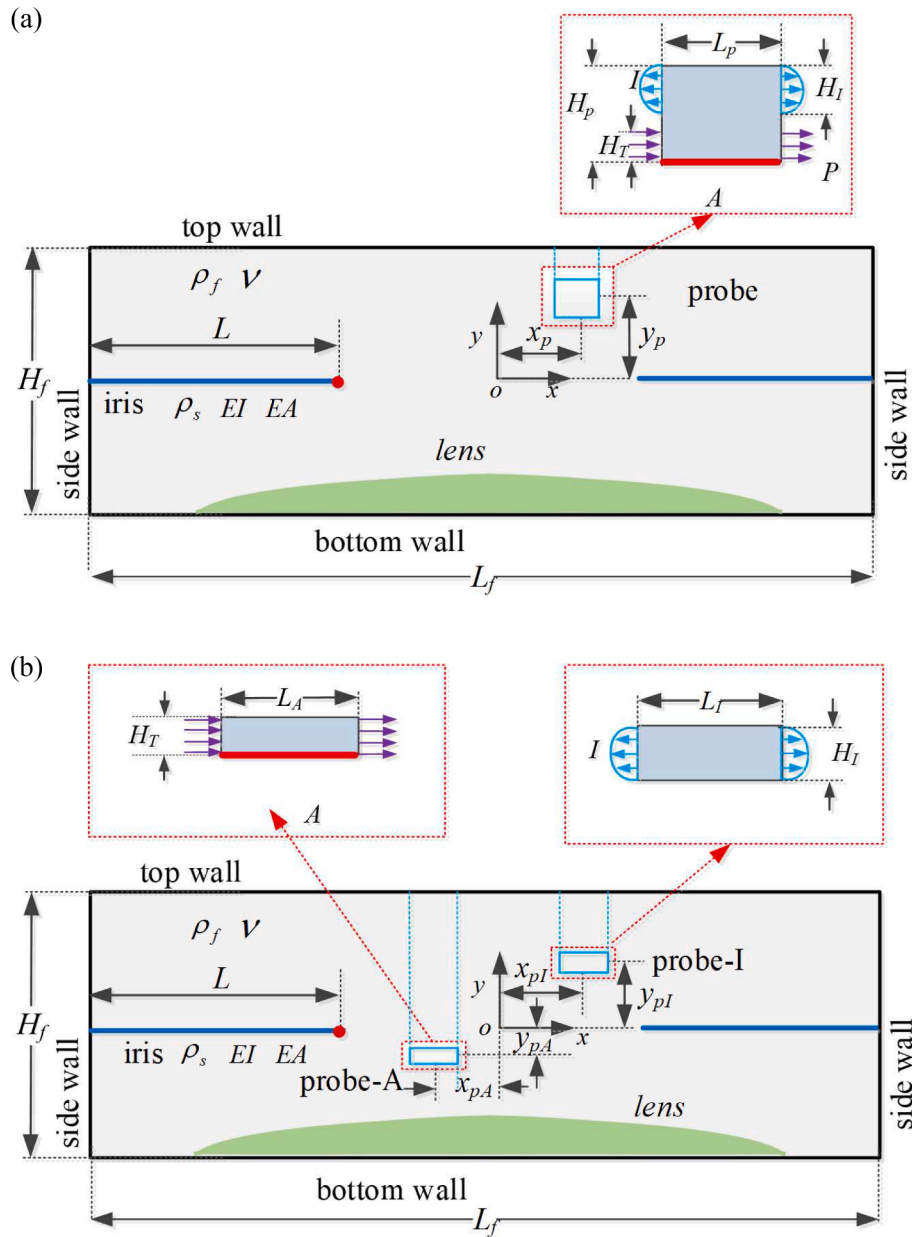
Fig. 1. Schematic of a simplified two-dimensional eye model for probe-iris interaction study during phacoemulsification-based cataract surgery with probe in T-I/A mode (not in scale): (a) coaxial probe operation case; (b) bimanual probe operation case, including the irrigation probe (probe-I) and aspiration probe (probe-A). The length of undisturbed iris is assumed to be L and the coordinate origin O locates at the center of the model. The parabolic-distributed light blue arrow defines the irrigation flow, and the purple arrow defines the probe torsional-operation-induced flow. The thick red line realizes the continuous aspiration through the constant pressure, and the filled cyan area denotes the lens presence.

examine the influence of iris stiffness, presence of lens and probe type on the iris dynamics. Lastly, appropriate discussions are summarized, in corporation with the clinical operation.

3.1. Modes of iris dynamics

The iris dynamics under various probe locations are firstly explored in detail. Through a systematic series of simulations in a wide range of probe locations, three distinct dynamic modes for iris are identified, including the repulsion mode (RP) wherein the probe-induced flow repels the iris away from the probe, the attraction mode (AT) wherein the iris bends toward but does not touch the probe, and the adhesion mode (AH) wherein the iris adheres to the probe, as illustrated in Fig. 2. In the RP mode, two different patterns are observed, namely, the RP I (see

Fig. 2(a)) and RP II(see Fig. 2(b)) modes, characterized by the I/A flow repelling the disturbed iris on the same and opposite side of the probe, respectively. In both the AT (as depicted Fig. 2(c)) and AH (illustrated in Fig. 2(d) and (e)) modes, the iris is forced to bend towards the probe, which increases the risk of the iris. In particular, in the AH mode, the strong attraction of the probe-induced flow attracts the iris tip or midriff adhering to the probe in the AH I and AH II modes, respectively, which may cause severe damage to the iris, as depicted in Fig. 2(d) and (e).

Representative cases are discussed first to reveal the iris dynamics in different modes. Velocity and pressure fields, alongside the fluid force exerted on the iris, are examined. Considering the established positive correlation between maximum stress/strain and tissue failure/damage [49,50], strain distribution along the iris is analyzed for insights into its local stretch, with detailed calculations referenced in APPENDIX B, to

Table 2
Definition and chosen values of key dimensionless parameters used in this study.

Dimensionless parameter	Definitions	Baseline values or ranges
Length of fluid domain	$L_f^* = L_f/L$	3 [9]
Height of fluid domain	$H_f^* = H_f/L$	1
Coaxial probe horizontal location	$x_p^* = x_p/L$	−0.9~0
Coaxial probe vertical location	$y_p^* = y_p/L$	−0.3~0.3
Coaxial probe length	$L_p^* = L_p/L$	0.3 [39]
Coaxial probe height	$H_p^* = H_p/L$	0.3
Bimanual probe-A horizontal location	$x_{pA}^* = x_{pA}/L$	−0.9~0
Bimanual probe-A vertical location	$y_{pA}^* = y_{pA}/L$	−0.3~0.3
Bimanual probe-I horizontal location	$x_{pI}^* = x_{pI}/L$	−0.6, 0, 0.6
Bimanual probe-I vertical location	$y_{pI}^* = y_{pI}/L$	0.3
Irrigation port length of bimanual probe	$L_I^* = L_I/L$	0.3
Irrigation port height	$H_I^* = H_I/L$	0.15
Aspiration port length of bimanual probe	$L_A^* = L_A/L$	0.3
Aspiration port height	$H_A^* = H_A/L$	0.1
Irrigation jet velocity	$V_I^* = V_I/V_T$	1.47 [39]
Horizontal position of iris tip	$x_{tip}^* = x_{tip}/L$	–[a]
Vertical position of iris tip	$y_{tip}^* = y_{tip}/L$	–
Mean vertical position of the iris tip[b]	$\bar{y}_{tip} = \bar{y}/L$	–
Fluid loading	$F_f^* = F_f/\rho_f V_T^2$	–
External force per unit volume	$f_e^* = f_e L/V_T^2$	–
Bending stiffness	$EI^* = EI/\rho_f V_T^2 L^3$	0.00425~0.085, baseline value 0.017 [9,25]
Stretching stiffness	$EA^* = EA/\rho_f V_T^2 L$	6.217~124.345, baseline value 24.869 [9,25]
Mass ratio	$m^* = \rho_s/\rho_f L$	0.091
Iris' position	$\mathbf{X}^* = \mathbf{X}/L$	–
Lagrangian coordinate	$s^* = s/L$	–
Reynolds number of T mode	$Re_T = V_T L/\nu$	1560 [25,30,39,40]
Reynolds number of I/A mode	$Re_I = V_I L/\nu$	2294 [39]
Velocity	$\mathbf{u}^* = \mathbf{u}/V_{max}$	–
Pressure	$p^* = p/\rho_f V_{max}^2$	–
Time	$t^* = V_{max} t/L$	–
Frequency[c]	$f^* = f/f_N = 2\pi f L^2/(k_1^2 \sqrt{EI/\rho_s})$	4.9 [40,41]

[a] The symbol "–" indicates that the corresponding parameter is updated during the simulation.

[b] $\bar{y}$ defined as the mean value of iris-tip maximum and minimum vertical positions y_{tip}.

[c] f_N is the first natural frequency of the flexible iris in vacuum, defined as $f_N = k_1^2 \sqrt{EI/\rho_s}/2\pi L^2$, and $k_1 = 1.8751$ [42].

aid in determining the operation modes more likely to cause iris damage. Fig. 3 depicts RP deformation mode of iris in different operating scenarios, with the coaxial, bimanual and pure torsional probes located at $x_p^* = -0.35$ and $y_p^* = -0.2$, where pure torsion means only torsional vibration is activated (refer to Ref. [30]). It suggests that the I/A flow works as the dominant factor influencing the iris dynamics. Specifically, in both the coaxial and bimanual cases (see Fig. 3(a1) and (a2)), an intense flow jet resulting from the I/A flow directly acts on the iris' forepart, and further pushes the iris downwards. Consequently, despite the upward attracting force at the iris' tip (see Fig. 3(b1) and (b2)), the iris develops into the RP II mode. On the contrary, in the pure torsional probe case in Fig. 3(a3), the iris is in the RP I mode and vibrates in the first bending mode around its mean deflected position. The vibration is

attributed to the alternating pulling and pushing flow induced by the probe. This obvious oscillation is not observed in the coaxial and bimanual probe cases, where the dominated I/A flow pushes the iris rapidly touching the chamber lower boundary. Additionally, the intense I/A flow significantly increases the stretching strain on the iris, thus affecting the iris' safety, especially at the root region of the iris, as seen in the comparison among Fig. 3(c1), (c2) and (c3). Therefore, special attention should be paid here to minimize the iris risk during phacoemulsification procedures.

Varying probe's location significantly alters the iris' dynamics. Relocating the probe to $x_p^* = -0.5$ and $y_p^* = 0.25$ in the coaxial case and $x_p^* = -0.4$ and $y_p^* = 0.25$ in the bimanual and torsional cases significantly alter the iris dynamics, with coaxial transitioning to AH mode and bimanual and torsional shifting to AT mode, respectively. In the coaxial case (see Fig. 4(a1)), the aspiration port attracts the iris' forepart upward, while the blowing of the probe's irrigation port directly induces high pressure on the iris' upper surface(see Fig. 4(b1)), causing the iris to move downward and bear severe stretching (see Fig. 4(c1)). These two time-varying forces alternately affect the iris, making it flapping around its mean position. A similar pattern is observed in the bimanual case (see Fig. 4(a2)), where the iris is mainly deflected by the I/A flow and vibrates due to the excitation of the torsional port. Even in the absence of I/A flow, the iris still undergoes bending motion towards the probe, caused by the attractive force of oscillatory torsional jets, see Fig. 4(a3). Nevertheless, the stretching of the iris is considerably reduced, thereby enhancing its safety, as shown in Fig. 4(c3). It should be noted that the maximum strain consistently manifests at the iris root, as illustrated in Fig. 4. This underscores the necessity for extra care on iris root during surgery, to relieve stretching injury and the possibility of iris detachment. If the probe approaches the iris further, the aspiration port's attraction to the iris is greatly intensified, causing the iris to enter the AH state. Given the similarity of the iris dynamics in AH and AT modes, albeit with different force intensities on iris, the comprehensive discussion can refer to that of AT mode to avoid repetition.

The mode distributions for three distinct probe configurations i.e., coaxial, bimanual and torsional ones, are presented in Fig. 5 for the probe operating with the following parameters: $Re_T = 1560$, $Re_{IA} = 2294$, $m^* = 0.091$, $EI^* = 0.017$, $EA^* = 24.869$, and $f^* = 4.9$. The probe position varies with a spatial increment of $d/L = 0.1$ in both the x^* and y^* directions, which is decreased to $d/L = 0.05$ near mode boundaries to precisely capture the transitions between different modes. Additionally, blank regions are intentionally left to prevent overlap between the iris and probes. Given the problems' symmetry, wherein the probe-I remains fixed at $x_{pI}^* = 0$ and $y_{pI}^* = 0.3$ in bimanual case, here we only display the left half of the simulation domain. The observations indicate that, in all three cases, the iris is generally drawn towards the probe when it is situated within the contactable zone of the iris, defined as the region that the flexible iris can geometrically touch the probe (represented by the red dashed arc). More specifically, all irises develop into the AH mode (represented by red squares) in nearly the entire iris-probe contactable zone, with the exception of the lower- and upper-right regions for the coaxial case, and the upper-right region for the bimanual case. In contrast, the iris is mostly in the RP mode (represented by blue dots) when the probe is positioned outside the contactable zone. In the coaxial situation (Fig. 5(a)), the RP mode marginally crosses the upper and lower contactable zone boundaries and enters the iris-probe contactable zone. In the bimanual scenario (Fig. 5(b)), a small RP mode zone as well as a tiny AT mode zone is situated within the contactable zone, primarily through the upper portion of the contactable boundary. These distinct iris dynamics are mainly resulted from different I/A flows induced by the probes. From a clinical perspective, the coaxial probe is preferable for cataract surgery given that it offers a larger safe RP region for probe operation, especially in the concerned area underneath the iris. Compared to the mode distribution in the T mode (as shown in Fig. 5(c)), the inclusion of I/A flow in two I/A-T scenarios greatly increases the iris' risk by enlarging dangerous AH zones, while mostly shrinking the semi-
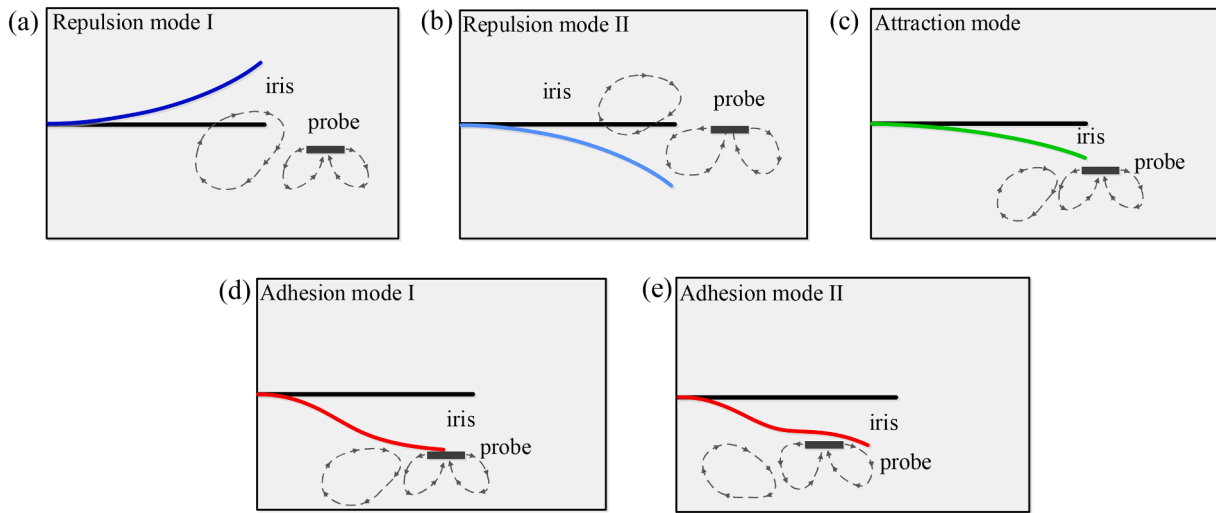
Fig. 2. Patterns of the iris dynamics in three typical modes: repulsion (RP) mode I (a) and II (b); attraction (AT) mode (c); adhesion (AH) mode I (d) and II (e). The black line represents the iris' undisturbed shape, the dark blue line in (a), light blue line in (b), the green line in (c), and the red lines in (d) and (e) are the mean positions of the deformed iris in corresponding modes. The dashed black lines with arrows illustrate the flow direction in the Coaxial T-I/A case, providing insight into the interaction between flow and iris. In RP II, the direct impact of I/A flow on the iris results in a downward deformation. In contrast, the clockwise flow induced by the anticlockwise I/A flow on the probe's left side causes an upward repulsion of the iris, leading to RP I. When the probe is positioned beneath the iris, the combined clockwise and anticlockwise flows generate a downward flow jet, attracting the iris towards the probe and leading to the development of AT or AH mode based on the amplitude of attraction force. As the probe is placed further inside, the irrigation flow from the probe's right-side initiates shearing and attracts the iris, resulting the iris developing into AH II mode.
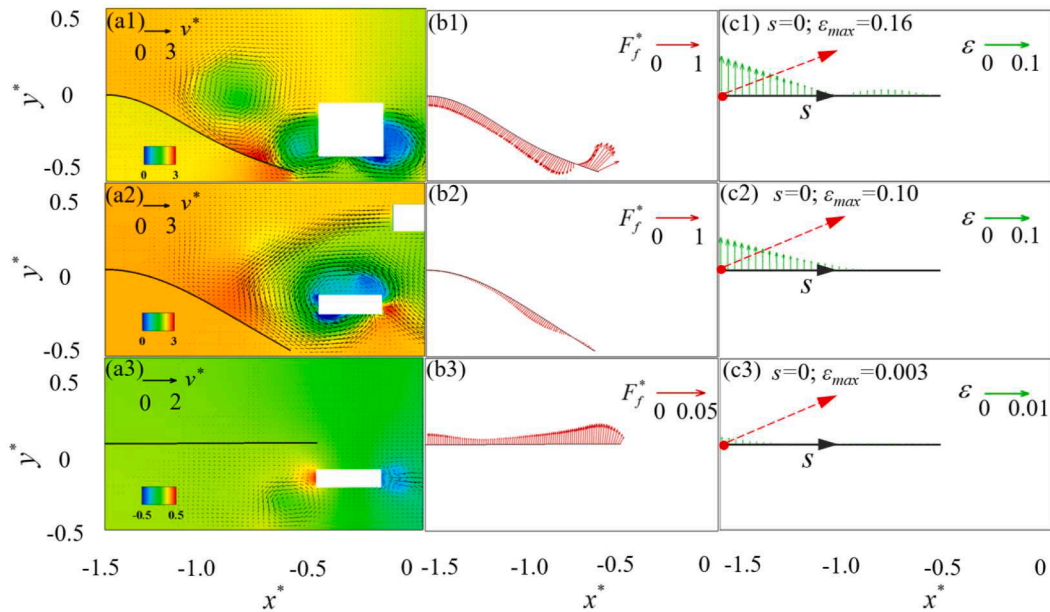
Fig. 3. Pressure (p^*) contour and velocity(v^*) field around the iris (1st column) along with the fluid loading (F_f^*, 2nd column) and the strain distribution (3rd column) along the iris at one selected instance, for the representative coaxial case (1st row), bimanual case (2nd row) and pure torsional case (3rd row), respectively, with the probe located at $x_p^* = -0.35$ and $y_p^* = -0.2$. The iris segment experiencing the maximum strain is marked by a solid red dot, accompanied by a label indicating both its location and the corresponding strain value. The black lines represent the position of the disturbed iris.

dangerous AT zones.

To reveal the sole contribution of the I/A flow, a comparative study is performed, in which the coaxial probe is operated in only I/A mode. Fig. 5(d) shows the resultant mode distribution in I/A mode. The similarity with Fig. 5(a) (T-I/A) indicates that the I/A flow has a dominating role in the mode distribution. Regarding the bimanual case, despite the effect of probe-A, the location of probe-I also affects iris dynamics, and a more detailed discussion on the effect of probe-I's location can be found in the subsequent Section 3.4. Additionally, the influence of the

torsional probe frequency on iris dynamics is examined, revealing its minimal effect on the mode distribution compared to the I/A flow. Further details are provided in APPENDIX C.

In the following sections, motivated by the clinical implications, the effects of iris stiffness, lens presence and I/A type on the iris dynamics are studied by varying the corresponding governing parameters. The related results on the iris dynamics are presented and discussed accordingly.
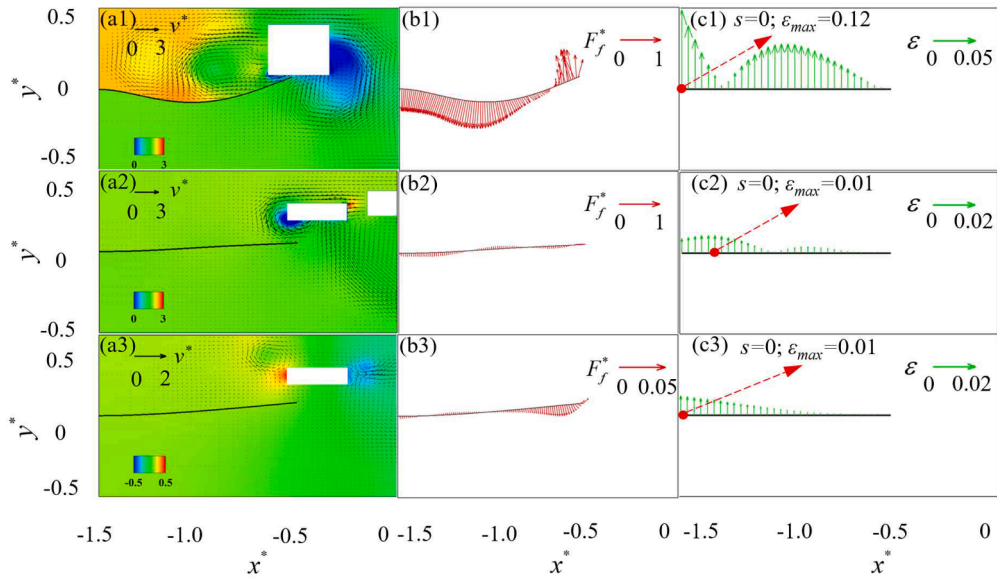
Fig. 4. Pressure (p^*) contour and velocity(v^*) field surrounding the iris (1st column) together with the fluid loading (F_f^*, 2nd column) and the strain distribution (3rd column) along the iris for the AH-mode representative coaxial case (1st row), AT-mode representative bimanual case (2nd row) and pure torsional case (3rd row), with the probe located at location $x_p^* = -0.5$ and $y_p^* = 0.25$ for coaxial case and $x_p^* = -0.4$ and $y_p^* = 0.25$ for bimanual and torsional cases, respectively. The iris segment experiencing the maximum strain is marked by a solid red dot, accompanied by a label indicating both its location and the corresponding strain value. The black lines represent the position of the disturbed iris.
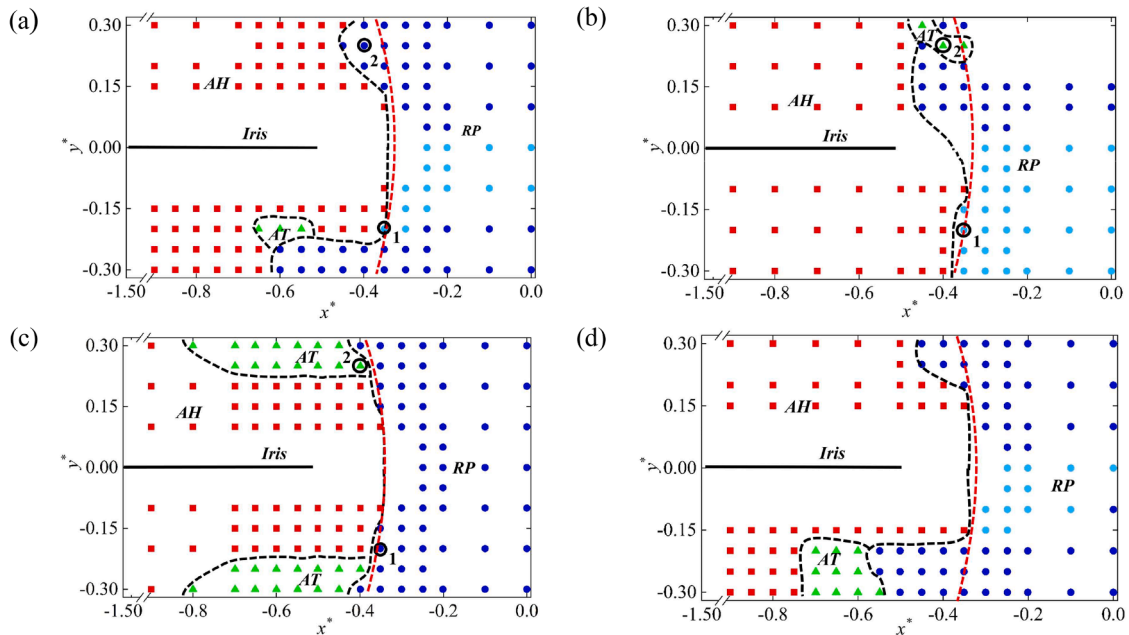
Fig. 5. Spatial distributions of the three deformation modes: (a) the coaxial probe operation case; (b) the bimanual probe operation case; (c) the torsional probe operation case and (d) the coaxial probe operation case of only I/A. The symbols ●, ●, ▲ and ■ denote the repulsion (RP I), repulsion (RP II), attraction (AT) and adhesion (AH) modes, respectively. The horizontal black solid line represents the undisturbed iris shape. The black dashed lines define the boundaries among different mode zones and the red dashed line describes the boundary of the location of the probe center, within which the iris can come into contact with the probe literally. The cases at representative locations, i.e., location1: $x_p^* = -0.35$ and $y_p^* = -0.2$ and location2: $x_p^* = -0.4$ and $y_p^* = 0.25$, are marked by the black circles.

3.2. Effect of iris stiffness

In this section, we examine the influence of iris stiffness on iris dynamics. Clinically, the prostate medication tamsulosin typically increases the risk of IFIS by softening the iris. In cataract surgery, pre- and perioperative injections of phenylephrine are commonly indicated to mitigate the IFIS risks via stiffening the iris. To investigate the influence of iris stiffness, the iris' elastic modulus r_E (defined as $r_E = E/E_{baseline}$,

where $E_{baseline}$ is the Young's modulus in baseline case) is halved and quadrupled to mimic the softened (usage of tamsulosin) and stiffened (usage of phenylephrine) iris in both the coaxial and bimanual conditions. Specifically, Fig. 6(a) and (c) illustrate the distribution patterns of the softened iris' three dynamics modes in coaxial and bimanual cases, respectively, while Fig. 6(b) and (d) display the distribution patterns of stiffened iris in both coaxial and bimanual cases. By contrasting the patterns of softened and stiffened iris, it is apparent that in the coaxial
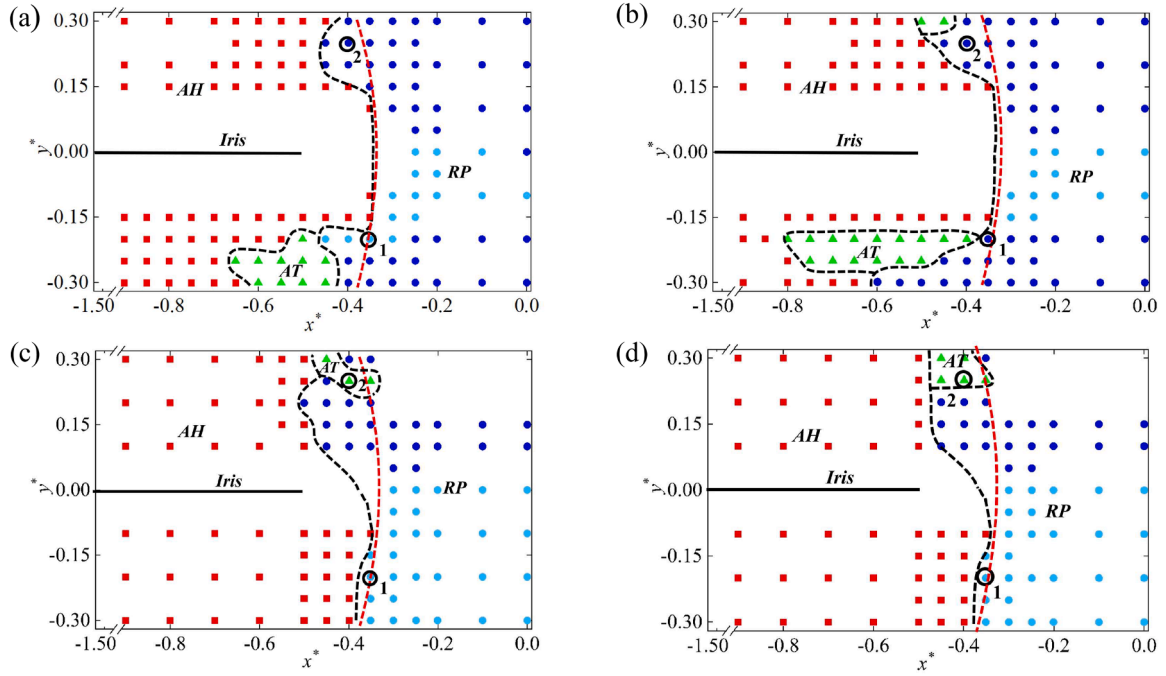
Fig. 6. Spatial distribution of the three typical dynamic modes in the x^*-y^* plane for the softened iris (with (a), (c) for coaxial and bimanual scenarios, respectively) and stiffened iris (with (b), (d) for coaxial and bimanual scenarios, respectively). Symbols ●, ●, ▲ and ■ denote RP I, RP II, AT and AH modes, respectively. The horizontal black solid line represents the undisturbed iris shape. The black dashed lines sketch the boundaries among different mode zones, whereas the red dashed line defines the iris-probe contactable zone.

case, increasing iris stiffness significantly narrows the dangerous AH mode region mainly by expanding the AT mode, particularly in the concerned area underneath the iris. While in the bimanual scenario, the distribution of modes remains essentially unchanged, with only minor shifts among AT, AH and RP in the upper region.

The variations of dimensionless mean vertical position ($\bar{y}_{tip}$) of the iris tip against the stiffness ratio r_E in the six selected cases at location 1 and location 2 (defined in Fig. 5) are plotted in Fig. 7. When the probe is operated at location 1 (see Fig. 7(a)), the iris deformation patterns in the coaxial case and the pure torsional case remain in the RP mode in the whole stiffening process. However, a sudden increase of $\bar{y}_{tip}$ appears in both cases, which is caused by the transition from RP II to RP I (see Fig. 2). This transition is also evidenced by comparison between the stiff and soft irises in coaxial (see Fig. 8(a)) and torsional (see Fig. 8(c)) cases. Unlike the coaxial case, the bimanual case does not undergo inter-RP mode transition. In this case, with the iris stiffening($r_E \geq 6.0$), the $\bar{y}_{tip}$

of iris increases significantly, and the iris no longer touches the lower boundary of the chamber, as depicted in Fig. 8(a). The intensified restoring force of stiffer iris moves the iris tip towards its undistributed location ($\bar{y}_{tip}=0$).

In the cases where the probe is operated at location 2, with the stiffness gradually increasing in all three scenarios, the iris tip initially moves downward and then approaches its undisturbed location, see Fig. 7(b). The restoring process observed is primarily attributed to the increased elastic force in iris due to iris stiffening. However, the stiffened iris' increased resistance to deformation results in a larger downward rigid-body motion even with a smaller deformation. Take the coaxial case as an example, see Fig. 9, the softer ($r_E=0.5$) and stiffer ($r_E=3.0$) irises experience distinct deformations, but the softer iris tends to deform upwards due to the attracting force induced by the probe's aspiration, while the stiffer iris tends to bend downward entirely.
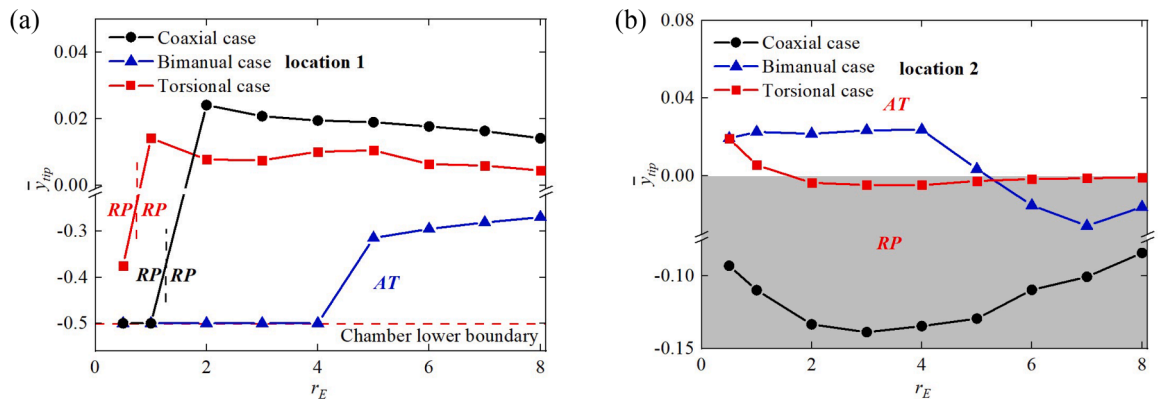
Fig. 7. Effects of tip deflection vs stiffness: dimensionless mean vertical value $\bar{y}_{tip}$ of the iris tip for six representative cases at location 1 (a) and 2 (b) for the coaxial, the bimanual probe and the torsional probes(defined in Fig. 5), with the stiffness proportion coefficient r_E ranging from 0.5 to 8.0, in which RP, AT and AH represent the repulsion, attraction and adhesion mode, respectively.
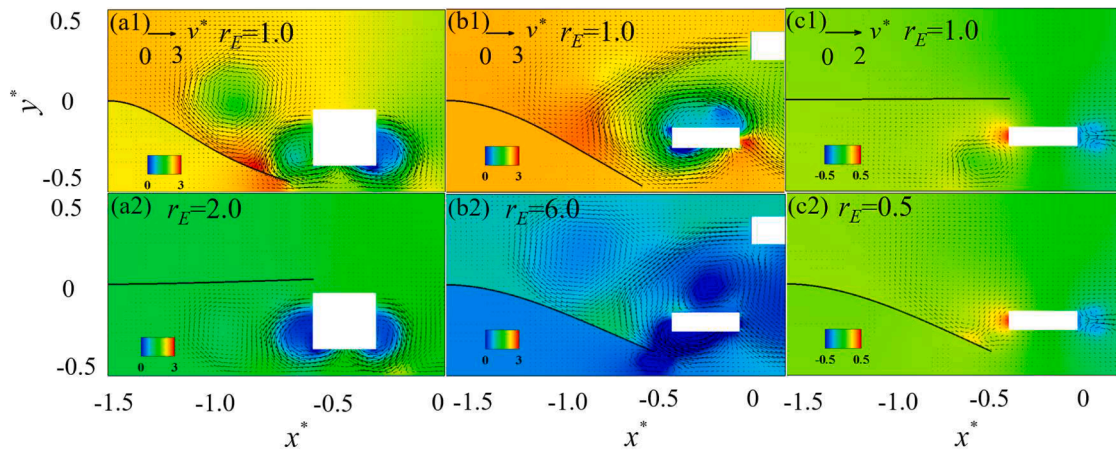
Fig. 8. Effects of flow fluid vs stiffness: pressure (p^*) contours, velocity(v^*) fields, and the instant position of the distributed iris at location 1 for coaxial case with r_E=1.0 (a1) and r_E=2.0 (a2), bimanual case with r_E=1.0 (b1) and r_E=6.0 (b1), and torsional case with r_E=0.5 (c1) and r_E=1.0 (c1). The black line denotes the position of the distributed iris, and the arrow represents the velocity vector.
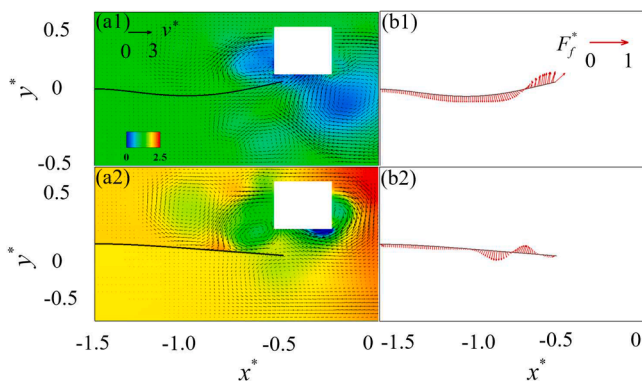
Fig. 9. Pressure (p^*) contours and velocity (v^*) fields around the iris (1st column) as well as the fluid loading (F_f^*, 2nd column), for the RP-mode representative coaxial case at location 2 (defined in Fig. 5(a)) with the stiffness proportion coefficient r_E=0.5 (1st row) and r_E=3.0 (2nd row). The black lines represent the position of the disturbed iris. The black dash line denotes the streamline, and the arrow represents the velocity vector.

3.3. Effect of the presence of lens

The presence of lens affects the iris dynamics. In the initial stage of the surgery, when the lens has not yet been sculpted and removed, the presence of the lens may produce a significant effect on the iris dynamics. To explore this geometric influence, we further conducted

additional simulations with lens (the detailed geometrical information can be found in [9]). The mode distributions with lens presence are presented in Fig. 10(a) and (b) for coaxial and bimanual cases, respectively, where the filled cyan area represents the lens. Compared with the baseline case in Fig. 5(a) and (b), it can be observed that the mode boundaries only slightly move in the upper region near the probe-iris contactable boundary. Specifically, in the coaxial situation, the AH-RP boundary shifts in the direction to AH, whereas in the bimanual case, the AT zone somewhat widens by narrowing RP zone. This slight boundary movement indicates that the mode distributions for probe operation in baseline cases (see Fig. 5) are also suitable for the scenario with lens presence, with the exception of the small upper region around the contactable boundary.

The velocity and pressure fields, iris velocity distribution, and strain along the iris are examined at specific instances for both coaxial and bimanual scenarios at location 2, taking into account the lens presence, as depicted in Fig. 11. Upon comparing the scenarios with and without lens (as depicted in Fig. 4(a) and (b)), it is evident that both cases with the lens maintain their initial modes, with the coaxial case in RP mode and bimanual case in AT mode. However, compared to the scenarios without lens (see Fig. 4(a1)), the existence of lens enhances the flow complexity, particularly in the coaxial case where more vortices are observed (see Fig. 11(a)). This increased flow complexity may reduce the controllability and operability of the lens fragment removal during the phacoemulsification. However, the lens presence does not greatly affect the strain amplitude experienced by the iris, which remains similar to the cases without lens (as shown in Fig. 3(c) and Fig. 4(c)).
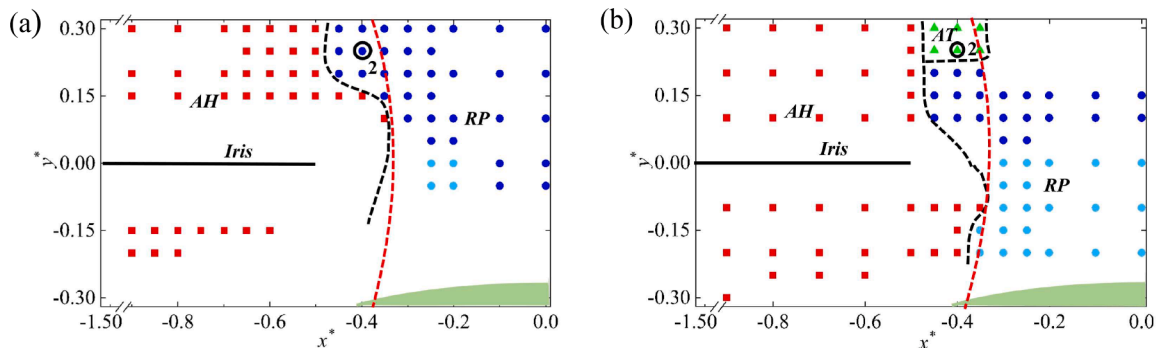
Fig. 10. Spatial distribution of the three typical dynamic modes in the x^*-y^* plane for coaxial (a) and bimanual (b) scenarios. Symbols ●, ●, ▲ and ■ denote RP I, RP II, AT and AH modes, respectively. The horizontal black solid line represents the undisturbed iris shape. The filled brown area denotes the lens in the current region. The black dashed lines sketch the boundaries among different mode zones, whereas the red dashed line defines the iris-probe contactable zone.
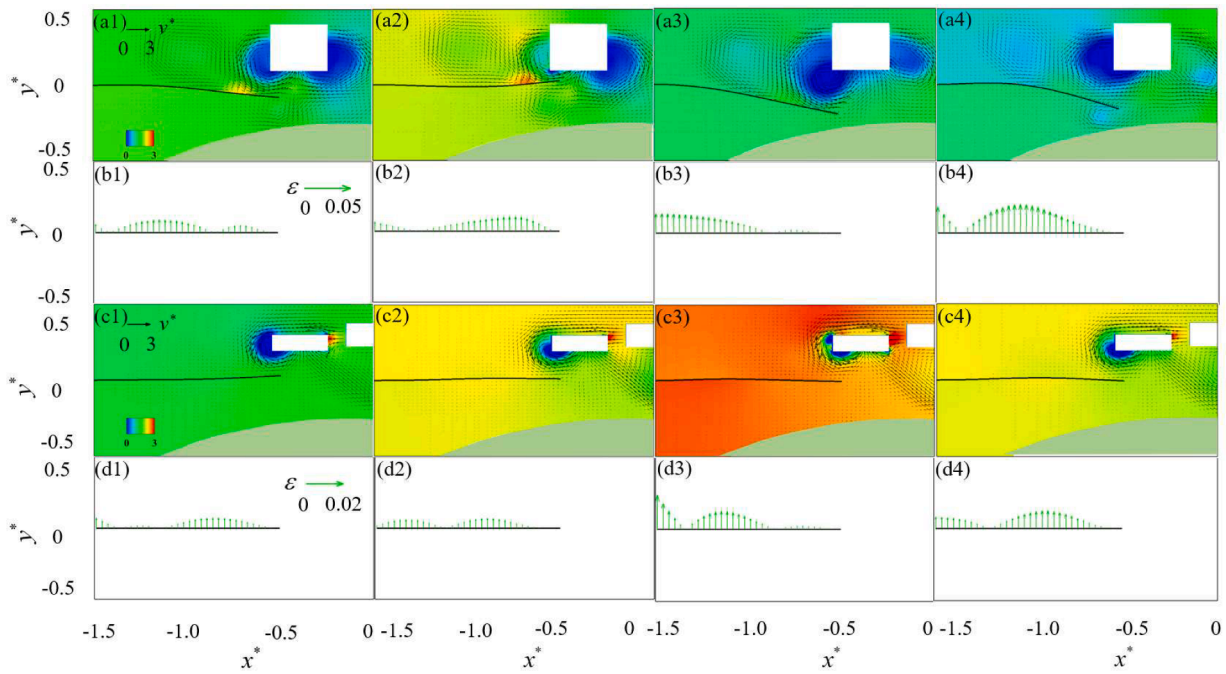
Fig. 11. Pressure (p^*) contours, velocity(v^*) fields, and the instant position of the distributed iris at typical instances for the coaxial case in the RP mode (a) and the bimanual case in AT mode (c) at location 2, with the presence of lens. Strain distribution along the iris is depicted for the coaxial (b) and bimanual (d) cases, respectively. The black line denotes the position of the distributed iris, and the arrow represents the velocity vector. Results are compared with those without the lens (e.g., Fig. 3 and 4) for reference.

Additionally, the bimanual approach appears to be more favorable to the iris due to its lower strain amplitude, as demonstrated by the comparison between Fig. 11(b) and (d), which also applies to the scenarios without lens(see Fig. 3(c) and Fig. 4(c)).

3.4. Effect of probe-I location on mode distributions in bimanual case

In the bimanual case, the location of the probe-I may affect the iris dynamics. Hence a comparative study is conducted, in which the probe-I is placed above the iris at two different horizontal locations $x_{pI}^*=-0.6$ and 0.6 but the same vertical location $y_{pI}^*=0.3$. Fig. 12 shows the resulted mode distribution maps for various probe-I locations. Through comparison with the baseline case in Fig. 5(b), it is observed that the horizontal location of probe-I does affect the distribution of the iris dynamics modes. In particular, when the probes are positioned at the same side, as depicted in Fig. 12(a), relatively large RP and AT zones extend into the probe-iris contactable region, indicating that it is safer for iris to operate the probe-A with the same side of probe-I.

3.5. Movement of mode boundaries

Three distinct modes for iris dynamics, i.e., RP, AT, and AH modes, are identified when probes operate at various locations. With placing the probe in the RP mode zone, the iris is repelled by the probe, whereas it is attracted when the probe is placed in the AT or AH mode zones, and it becomes adhesive to the probe if the probe is in the AH mode zone. When adjusting the iris stiffness and I/A strength, altering operation probe type and sculpting the lens, the spatial changes for these mode distributions are schematically described in Fig. 13 and compared with the iris' mode distribution in the pure T mode (shown in Fig. 5).

Through comparison between the mode distributions in coaxial and bimanual cases (see Fig. 13(a) and (b), respectively), it is observed that the safe RP mode region in the coaxial case is generally larger than that in the bimanual case, regardless of the variations of iris stiffness. Particularly in the region beneath the iris where the probe predominantly operates during surgery, the iris is found to be primarily in the vulnerable AH mode for the bimanual scenario. In contrast, in the
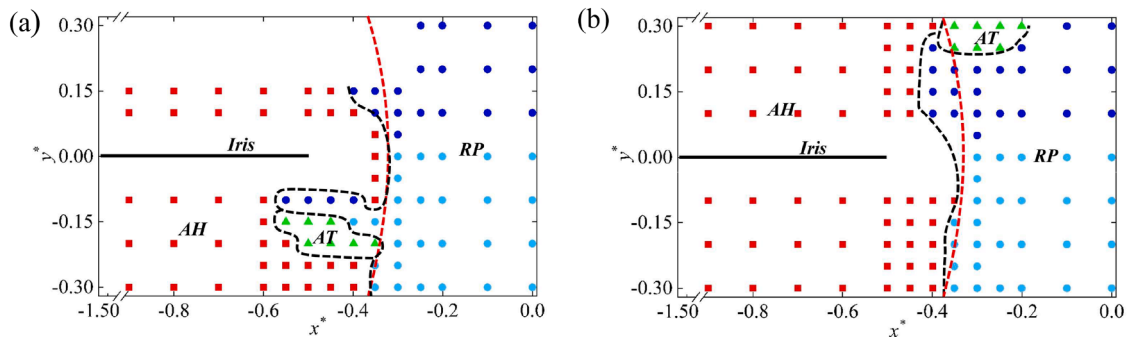
Fig. 12. Distribution of the three typical deformation modes in the x^*-y^* plane for the bimanual cases with probe-I located at $x_{pI}^*=-0.6$ and $y_{pI}^*=0.3$ (a) and $x_{pI}^*=0.6$ and $y_{pI}^*=0.3$ (b). The symbols ●, ●, ▲ and ■ denote the repulsion (RP I), repulsion (RP II), attraction (AT) and adhesion (AH) modes, respectively. The horizontal black solid line represents the undistributed iris shape. The red dashed line indicates the perimeter of the area where the probe center can physically come into contact with the iris. The upper-right blank region in (a) is due to the data missing to avoid overlap between probe-I and probe-A.

Fig. 13. Sketch showing the effects of iris stiffness, probe type, I/A flow and lens presence on the spatial distribution of the three dynamic modes for the coaxial case (a) and bimanual case (b). The purple, black and light blue arrows indicate the zone boundary moving direction due to iris stiffing, I/A decreasing and lens presence, respectively, and their length reflects the changing magnitude. The solid red lines define the boundaries between AT and AH modes, and the solid green lines represent the boundaries between RP and AH (or AT) modes. The thin dotted green and red lines indicate the boundaries among different mode zones for the probe T operation mode, whereas the red dashed line defines the iris-probe contactable zone.

coaxial case, the iris experiences a considerably larger semi-safe AT and safe RP mode, while the damaging AH zone beneath the iris contracts towards the root at approximately one fourth of the iris length in the baseline cases. It appears that the utilization of coaxial probe generates greater repulsion forces on the iris compared to the bimanual probe, leading to a reduced attracting force on iris in the coaxial scenario. The finding aligns with those of the earlier study [51], which proposed that the bimanual probe operation could reduce the pushing forces exerted by irrigation, thereby improving the efficacy of lens removal. This concurrently lessens the pushing forces acting on the iris compared to the coaxial probe operation. Consequently, a delicate balance needs to be struck between the efficiency of emulsification and the risk to the iris when determining the probe type. Generally, opting for a coaxial probe reduces the iris risk but may decrease the lens removal efficiency, whereas utilizing a bimanual probe produces the opposite effect. In addition, the coaxial case seems to be more sensitive to the variation of iris stiffness. To elaborate, in the coaxial case, iris stiffening significantly diminishes the damage AH mode zone mainly by enlarging the AT mode zone, particularly noticeable in the region beneath the iris. In particular, the AT/AH boundary shifts inward, covering one-fourth of the iris length, as the iris stiffness quadrupled (refer to Fig. 6). As for the bimanual probe case, the boundary of the AH mode region is relatively stable, and only a tiny upper region of the iris transits from RP mode to AH one. Taken together, these findings indicate the coaxial probe may be more optimal for cataract surgery, primarily owing to its expanded safe operational space underneath the iris.

Meanwhile, the comparison with the pure T mode pattern (denoted by the thin dotted green and red lines) indicates that I/A induced flow tends to increase the iris risks mainly by transiting the semi-safe AT mode into the dangerous AH one, while synchronously increasing the risk of stretching injury. Specifically, in the region beneath the iris of concern, the bimanual case illustrates that I/A flow markedly diminishes the operational AT and RP region, within the reach of the iris, as shown in Fig. 13(b), Fig. 6(b) and (c). In contrast, the coaxial case demonstrates that I/A flow extends the AH zone towards the iris tip, approximately one fifth of the iris length. Although the intensified I/A flow increases iris risks, it concurrently enhances the efficiency of lens removal and alleviates heat injury to the iris. Therefore, a balance exists between improving lens removal efficiency and mitigating IFIS risk as well as heat damage on iris in choosing I/A strength. The study also reveals that, in both coaxial and bimanual cases, when the probe is positioned centrally in the eye and dose not overlap with the iris tip, the iris tends to be repelled. Conversely, when the probe and iris tip have significant overlap, the iris is attracted, which increases the risk of injury. Therefore, it is better to place the probe outside the iris-probe contactable zone to mitigate the iris damaging risks. Furthermore, there is an elevated risk of iris root stretching injury in both coaxial and bimanual cases, as shown in Fig. 3(c) and Fig. 4(c). Surgeons should be operated with caution during cataract surgery to mitigate this risk.

4. Conclusions

In this study, we utilized an FSI numerical model to examine IFIS mechanism during the mechanical interaction between the iris and the probe-induced flow in the phacoemulsification-based cataract surgery. Two probe configurations, coaxial and bimanual, are assessed. The dynamics of the probe-fluid-iris system have been thoroughly investigated by evaluating the effects of several key factors, including probe type and position, I/A strength, iris stiffness, and the presence of lens. The major findings are summarized as follows:

Three distinct dynamics modes for iris, including the RP, AT and AH modes, were identified in both the coaxial and bimanual probe-operation cases. Optimal probe placement in the central eye region results in the repulsion of the iris (RP mode), while caution is advised against positioning the prove above or beneath the iris to prevent adherence (AH mode). I/A-induced flows increase iris risk by enhancing stretching strain, shifting the semi-safe AT zone to the damaging AH zone, particularly in bimanual probe operations. Therefore, in high-risk cases, stabilizing iris dynamics by reducing I/A strength is recommended, although it comes at the expense of decreased lens removal efficiency and increased risk of iris heat injury due to weakened flow circulation.

The effects of several key parameters, including iris stiffness, I/A probe type as well as lens presence on the distribution of the three dynamics modes and the corresponding iris dynamics were also investigated. When the iris becomes stiffer, the damaging AH mode region shrinks, mainly by expanding the semi-safe AT region in the coaxial probe case. In contrast, the AH mode remains relatively stable in the bimanual case with the stiffness. A stiffer iris aids recovering the deflected iris to its undistributed position, lowering the risk of damage. These findings offer mechanical support for the effectiveness of intra-cameral phenylephrine in mitigating IFIS risk. In addition, the coaxial probe, compared to the bimanual probe, was found more suitable for cataract surgery to alleviate the iris damaging risks by enlarging the operation space, albeit at the expense of the nuclear removal efficiency. Hence, a delicate balance exists in choosing the phaco probe types, considering both the phacoemulsification efficiency and the iris risk.

The study on the effect of lens presence indicates that its presence slightly affects the iris' mode zones, primarily within the non-major region of probe operation. However, it reduces the removal efficiency of the lens due to the increased flow complexity, particularly in the coaxial case. Furthermore, the lens presence appears not greatly affect

the strain amplitude experienced by the iris.

From a clinical viewpoint, it is safe for the iris to operate the probe within the RP mode zone, mainly in the middle portion of the anterior chamber and out of reach of the iris. The risk of IFIS can be reduced by using the medicine phenylephrine (stiffening the iris), decreasing the I/A strength and adopting the coaxial device. This work can provide new physical insights into the mechanisms of IFIS and give some guidance to optimize the surgical protocol.

Here, the current study still confronts several limitations, encompassing a two-dimensional numerical model, a simplified anterior chamber geometry, and the consideration only of the probe's torsional-irrigation/aspiration combined mode. However, despite these constraints, the study's outcomes yield valuable insights into the interaction between the probe and the iris, notably contributing to our understanding of the physical mechanism of IFIS. Nevertheless, further research is warranted to deepen our understanding of the IFIS mechanism. Subsequent investigations will address these limitations by exploring more realistic scenarios, specifically through three-dimensional simulations with realistic eye modeling. Additionally, the upcoming study intends to investigate iris dynamics under ultrasound power modulations, explore iris behavior in the probe's longitudinal-irrigation/aspiration combined mode, and evaluate the efficacy of IFIS mitigation using the Malyugin ring.

CRediT authorship contribution statement

Zhaokun Wang: Conceptualization, Methodology, Investigation, Visualization, Formal analysis, Writing – original draft. **Chenglei Wang:** Conceptualization, Methodology, Investigation, Writing – review & editing. **Fuwang Zhao:** Writing – review & editing. **Feng Ren:** Writing – review & editing. **Xiaoyu Luo:** Conceptualization, Writing – review & editing. **Hui Tang:** Conceptualization, Methodology, Resources, Investigation, Writing – review & editing, Supervision.

Declaration of competing interest

The authors declare that they have no known competing financial interests or personal relationships that could have appeared to influence the work reported in this paper.

Data availability

Data will be made available on request.

Acknowledgments

Appendix A. Numerical method and verification

The LBM has been extensively used as an alternative numerical scheme for fluid flow simulations due to its advantages of computational efficiency, simplicity, and ease of parallelization [30,48,52-57]. Here, the multiple-relaxation-time lattice Boltzmann equation (MRT LBE) with the body force model [43,48,58,59] is employed.

$$f_\alpha(x + c_\alpha \Delta t, t + \Delta t) - f_\alpha(x,t) = -M^{-1}SM(f_\alpha(x,t) - f_\alpha^{eq}(x,t)) - M^{-1}(I - S/2)Mg_\alpha(x,t)\Delta t, \tag{A-1}$$

where $f_\alpha(x, t)$ is distribution function for particles with velocity c_α at the position x and time t, and Δt is the time increment. The first term on the right-hand side (RHS) of the equation is the collision operator, in which S is non-negative diagonal relaxation matrix and M is transformation matrix. The equilibrium distribution function f_α^{eq} [60] is defined as

$$f_\alpha^{eq} = w_\alpha \left[\rho_f + \rho_{f0} \left(\frac{c_\alpha \cdot u}{c_s^2} + \frac{(c_\alpha \cdot u)^2}{2c_s^4} - \frac{u^2}{2c_s^2} \right) \right], \tag{A-2}$$

where w_α is the weighting factor, and c_s is the speed of sound. ρ_{f0} is the mean mass density, which is usually set as 1. The body force that symbolized the structure's presence is denoted by the second component on the RHS of equation (A-1). Guo's force scheme [58] is adopted to impose the structure's existence

$$g_\alpha = w_\alpha \left(\frac{c_\alpha - u}{c_s^2} + \frac{c_\alpha \cdot u}{c_s^4} c_\alpha \right) \cdot f_e, \tag{A-3}$$

where f_e is the external force. The variables velocity u and mass density ρ_f can be calculated by

$$\rho_f = \sum_\alpha f_\alpha, u = \sum_\alpha c_\alpha f_\alpha + 1 \bigg/ 2f_e \Delta t, \tag{A-4}$$

A geometrically nonlinear finite element method with a co-rotational scheme [45] is adopted to solve the governing Eq. (3) for iris dynamics. This numerical strategy involves splitting the motion of the structure into two parts, namely, the large rigid motion and small pure deformation of the body, to separately resolve large-displacement and small-strain deformation. By introducing the co-rotational local and global coordinate systems, the geometrical nonlinearities of the structure are handled with the aid of coordinate transformation [30,45,61,62]. Specifically, in the co-rotational scheme, a local coordinate system moves with each discrete beam element, in which the element behaves linearly as described by the Bernoulli-Euler beam theory. And thus, geometrical nonlinearities are transferred into the coordinate transformation between the local and global coordinate systems. The Newmark method [63] is applied for time discretization, and the Newton-Raphson iteration [63] is adopted in each time step to reach the structure's dynamic equilibrium.

Furthermore, the interaction between the fluid flow and the iris is handled by using the direct-forcing immersed boundary method (IBM) [48,

64-68]. The interacting Lagrangian force density can be evaluated as

$$\boldsymbol{F}_f(\boldsymbol{s},t) = -2\rho_f \frac{\boldsymbol{U}(\boldsymbol{s},t) - \boldsymbol{u}(\boldsymbol{s},t)}{\Delta t}, \tag{A-5}$$

where $\boldsymbol{U} = \partial \boldsymbol{X}/\partial t$ is the iris velocity and $\boldsymbol{u}$ is the fluid velocity at the position of iris, which can be interpolated by $\boldsymbol{u}(\boldsymbol{s},t) = \int_{\Omega} \boldsymbol{u}(\boldsymbol{x},t)\delta(\boldsymbol{x} - \boldsymbol{X}(\boldsymbol{s},t))d\boldsymbol{x}$ using 4-points Dirac delta function δ [48].

The Lagrangian interaction force $\boldsymbol{F}_f$ is then spread onto the nearby Eulerian grids to enforce the no-slip and no-penetration boundary conditions on the iris surface

$$\boldsymbol{f}_e(\boldsymbol{x},t) = -\int_{\Gamma} \boldsymbol{F}_f(\boldsymbol{s},t)\delta(\boldsymbol{x} - \boldsymbol{X}(\boldsymbol{s},t))d\boldsymbol{s}, \tag{A-6}$$

More details about the current numerical framework are given in our previous works [30,53-57,69-71] and its validations can be found in our recent study [30,72,73].

To ensure the independence of the simulation results on the chosen grids and time steps, a convergence study is conducted on the selected baseline case of coaxial scenario, in which the coaxial probe is place at $x_p* = -0.3, y_p* = -0.1$ (close to the left iris) and operates in T-I/A mode. Three different configurations of grid and time-step resolutions are compared in Table A1. Fig. A1 depicts the time-dependence of $y_{tip}*$ (the vertical displacement of the left iris' tip) on the different lattice spacings and time steps. The consistent results indicate that $\Delta x = L/512$ and $\Delta t = L/25{,}600\ u$ in Set 2 is adequate to produce accurate results in the present simulations. Hence, $\Delta x = L/512$ and $\Delta t = L/25{,}600\ u$ were adopted in present study to maintain the computational accuracy without losing efficiency.

Table A1
Three sets of mesh and time step for the convergence study.

	Set 1	Set 2	Set 3
Mesh spacing (Δx)	$L/512$	$L/512$	$L/768$
Time step (Δt)	$L/51200u$	$L/25600u$	$L/25600u$
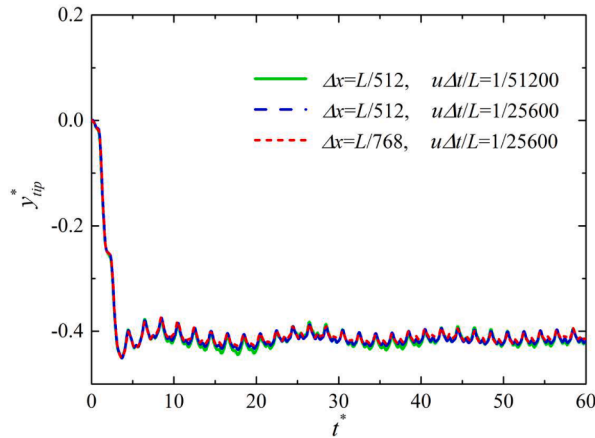
Fig. A1. Comparison of evolution of the vertical displacement $y_{tip}*$ of the iris tip.

Appendix B. Evaluation of the maximum strain on the iris

To assess the stretch of the iris, the maximum strain is calculated and used as a measure of iris safety. In the simulation, the iris undergoes tension and bending, as depicted in Fig. B1(a). Therefore, the strain calculating process is divided into two parts: the pure tension component (see Fig. B1(b)) and the pure bending component (see Fig. B1(c)). The tension strain is computed directly using the following equation:

$$\varepsilon_t = (L - L_0) / L_0 \tag{B-1}$$

where L_0 represents the initial length of the finite element representing the iris, and L is the length of tensed iris element.

The maximum bending strain occurs on the surface of the iris, which is furthest from the neutral axis at a distance of $h/2$, where h is the thickness of the iris. The bending strain can be determined as:

$$\varepsilon_b = h / 2\rho \tag{B-2}$$

where ρ is the radius of curvature for the iris element. It can be calculated from

$$\rho = 1 / \kappa = L_0 / (\theta_1 + \theta_2) \tag{B-3}$$

The maximum stretching appears on either the upper or the lower surface, with a constant amplitude that can be evaluated as:

$$\varepsilon = |\varepsilon_b| + |\varepsilon_b| \tag{B-4}$$
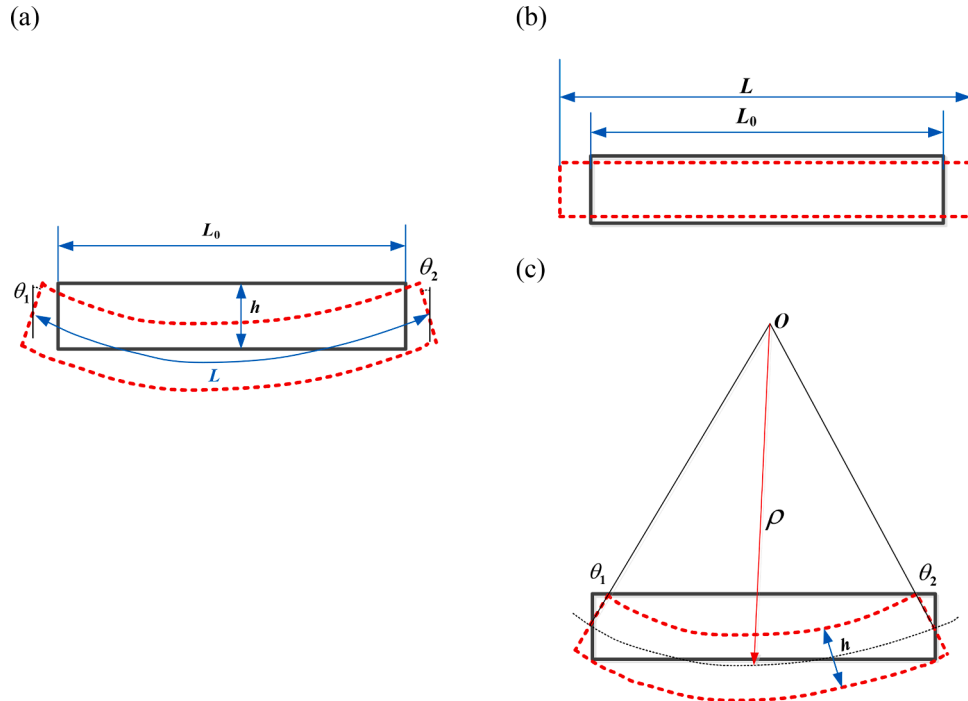
Fig. B1. The iris elemental deformation illustration for strain evaluation: (a) the combined deformation; (b) pure tension deformation; (c) pure bending deformation.

Appendix C. Effect of torsional probe frequency on iris dynamics

To explore the influence of probe operation frequency on the iris dynamics, we conducted simulations by varying its value from $f^* = 4.9$ to 9.8. Fig. C1 illustrates the distribution of the three dynamics modes as the probe is operated faster ($f^* = 9.8$) in T-I/A mode for coaxial probe. By comparing with the baseline case in Fig. 5(a), one can see that the probe frequency shows minimal effect on the mode distribution. This observation further suggests the dominant role of I/A flow in determining the mode distribution.
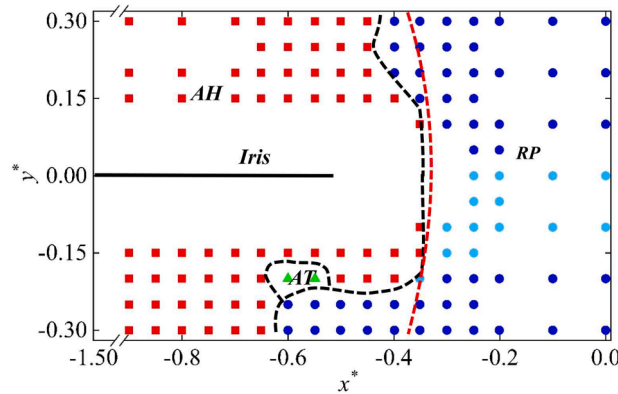
Fig. C1. Spatial distribution of the three typical dynamic modes in the x^*-y^* plane with a faster ($f^* = 9.8$) probe vibrations for coaxial scenarios, respectively. Symbols

,

,

and

denote RP I, RP II, AT and AH modes, respectively. The horizontal black solid line represents the undisturbed iris shape. The black dashed lines sketch the boundaries among different mode zones, whereas the red dashed line defines the iris-probe contactable zone.

References

[1] Brown NAP. The morphology of cataract and visual performance (in English) Eye 1993;7:63–7. https://doi.org/10.1038/eye.1993.14. Article vol.

[2] Gonzalez-Salinas R, Guarnieri A, Guirao Navarro MC, Saenz-de-Viteri M. Patient considerations in cataract surgery–the role of combined therapy using phenylephrine and ketorolac. Patient Prefer Adherence 2016;10:1795–801.

[3] Lawrence D, Fedorowicz Z, van Zuuren EJ. Day care versus in-patient surgery for age-related cataract. Cochrane Database Syst Rev 2015;2015(11):CD004242.

[4] SP M. GLOBAL data on visual impairments 2010. Bulletin World Health Organization; 2012 [Online]. Available, http://www.who.int/entity/blindness/GLOBALDATAFINALforweb.pdf?ua=1.

[5] Hassan B, Ahmed R, Li B, Noor A, Hassan ZU. A comprehensive study capturing vision loss burden in Pakistan (1990-2025): Findings from the Global Burden of Disease (GBD) 2017 study. PLoS One 2019;14(5):e0216492.

[6] Baltussen R, Sylla M, Mariotti SP. Cost-effectiveness analysis of cataract surgery: a global and regional analysis. Bull World Health Organ 2004;82:338–45.

[7] Kohnen T, Baumeister M, Kook D, Klaproth OK, Ohrloff C. Cataract surgery with implantation of an artificial lens. Deutsches Ärzteblatt Int 2009;106(43):695.

[8] Touma S, Antaki F, Duval R. Development of a code-free machine learning model for the classification of cataract surgery phases. Sci Rep 2022;12(1):2398.

[9] Qi N, Lockington D, Wang H, Hill NA, Ramaesh K, Luo X. Modeling Floppy Iris Syndrome and the Impact of Phenylephrine on Iris Buckling. Int J Appl Mech 2018; 10(5):1850048.

[10] Thanigasalam T, Thanigasalam SC, Reddy RA. Factors Associated with Complications and Postoperative Visual Outcomes of Cataract Surgery; a Study of 1,632 Cases. J Ophthalmic Vis Res 2015;10(4):375–84.

[11] Neff KD, Sandoval HP, de Castro LEF, Nowacki AS, Vroman DT, Solomon KD. Factors associated with intraoperative floppy iris syndrome. Ophthalmology 2009; 116(4):658–63.

[12] Storr-Paulsen A. Management of Intraocular Floppy Iris Syndrome (IFIS) in Cataract Surgery. InTech 2013. https://doi.org/10.5772/52328.

[13] Wang, Z. (2022). *Physical mechanism and control of intraoperative floppy iris syndrome* (PhD Thesis). Available at: https://theses.lib.polyu.edu.hk/handle/200/11694.

[14] Chang DF, Campbell JR. Intraoperative floppy iris syndrome associated with tamsulosin. J Cataract Refract Surg 2005;31(4):664–73.

[15] Pärssinen O. The use of tamsulosin and iris hypotony during cataract surgery. Acta Ophthalmol Scand 2005;83(5):625–6.

[16] Chang DF, Campbell JR. Intraoperative floppy iris syndrome associated with tamsulosin (in English) J Cataract Refract Surg Apr 2005;31(4):664–73. https://doi.org/10.1016/j.jcrs.2005.03.027. Article vol.

[17] Sparrow JM, Taylor H, Qureshi K, Smith R, Birnie K, Johnston RL. The Cataract National Dataset electronic multi-centre audit of 55 567 operations: risk indicators for monocular visual acuity outcomes. Eye 2012;26(6):821–6.

[18] Lockington D, Luo XY, Wang HM, Hill NA, Ramaesh K. Mathematical and computer simulation modelling of intracameral forces causing pupil block due to air bubble use in Descemet's Stripping Endothelial Keratoplasty: the mechanics of iris buckling (in English) Clin Exp Ophthalmol Mar 2012;40(2):182–6. https://doi.org/10.1111/j.1442-9071.2011.02653.x. Article vol.

[19] Lockington D, et al. Modelling floppy iris syndrome and the impact of pupil size and ring devices on iris displacement. Eye 2020;34(12):2227–34.

[20] Benjamin L. Fluidics and rheology in phaco surgery: what matters and what is the hype? Eye 2018;32(2):204–9.

[21] Kaji Y, Yamashita M, Sakakibara J, Oshika T. Visualization of irrigation fluid flow and calculation of its velocity distribution in the anterior chamber by particle image velocimetry. Graefe's Arch Clin Exp Ophthalmol 2012;250:1023–7.

[22] Abouali O, Bayatpour D, Ghaffariyeh A, Ahmadi G. Simulation of flow field during irrigation/aspiration in phacoemulsification using computational fluid dynamics," (in English). J Cataract Refract Surg Aug 2011;37(8):1530–7. https://doi.org/10.1016/j.jcrs.2011.02.026. Article vol.

[23] D. Bayatpour, O. Abouali, A. Ghaffarieh, G.J.M.e. Ahmadi, and physics, "In silico investigation of cornea deformation during irrigation/aspiration in phacoemulsification in cataract surgery," vol. 43, pp. 77–85, 2017.

[24] Jouzdani S, Amini R, Barocas VH. Contribution of different anatomical and physiologic factors to Iris contour and anterior chamber angle changes during pupil dilation: theoretical analysis (in English) Invest Ophthalmol Vis Sci Apr 2013;54 (4):2977–84. https://doi.org/10.1167/iovs.12-10748. Article vol.

[25] Amini R, Barocas VH. Reverse pupillary block slows iris contour recovery from corneoscleral indentation. J Biomech Eng 2010;132(7):071010.

[26] Heys JJ, Barocas VH, Taravella MJ. Modeling passive mechanical interaction between aqueous humor and iris (in English) J Biomech Eng-Trans ASME Dec 2001;123(6):540–7. https://doi.org/10.1115/1.1411972. Article vol.

[27] Heys JJ, Barocas VH. Computational evaluation of the role of accommodation in pigmentary glaucoma. Invest Ophthalmol Vis Sci 2002;43(3):700–8.

[28] Huang EC, Barocas VH. Active iris mechanics and pupillary block: steady-state analysis and comparison with anatomical risk factors (in English) Ann Biomed Eng Sep 2004;32(9):1276–85. https://doi.org/10.1114/B:ABME.0000039361.17029. da. Article vol.

[29] Huang EC, Barocas VH. Accommodative microfluctuations and iris contour (in English) J. Vision 2006;6(5):653–60. https://doi.org/10.1167/6.5.10. Article vol.

[30] Wang Z, et al. Simulation of fluid-structure interaction during the phaco-emulsification stage of cataract surgery. Int J Mech Sci 2022;214:106931.

[31] Kawamorita T, Shimizu K, Shoji N. Effect of hole size on fluid dynamics of a posterior-chamber phakic intraocular lens with a central perforation by using

[32] Wang Y, Shi X, Wei S, Yue C, Wang Z, Li X. Evaluation of flow field in the anterior segment during irrigation and aspiration in cataract surgery with three-dimensional computational simulation. Med Eng Phys 2022;99:103741.

[33] Wang X, Wang X. Simulation of fluid dynamics and turbulence during phacoemulsification using the new propeller turbo tip. BMJ Open Ophthalmol 2023;8(1):e001391.

[34] Aletti MCM. Mathematical modelling and simulations of the hemodynamics in the eye. Université Pierre et Marie Curie Paris; 2017. Doctor degree.

[35] Spirochkin Y. Hydrodynamic analysis and irrigation device design for the coaxial and bimanual phacoemulsification techniques in cataract surgery. Cataract surgery. IntechOpen; 2013.

[36] Connell BS, Yue DK. Flapping dynamics of a flag in a uniform stream. J Fluid Mech 2007;581:33–67.

[37] Hua R-N, Zhu L, Lu X-Y. Locomotion of a flapping flexible plate. Phys Fluids 2013; 25(12):121901.

[38] Izquierdo S, Fueyo N. Characteristic nonreflecting boundary conditions for open boundaries in lattice Boltzmann methods. Phys Rev E 2008;78(4):046707.

[39] Seibel BS. *Phacodynamics* (Mastering the tools and techniques of phacoemulsification surgery). USA: Slack Incorporated; 2005.

[40] Jirásková N, Rozsíval P. Phacoemulsification parameters: series 20000 legacy versus legacy with AdvanTec software and NeoSonix handpiece. J Cataract Refract Surg 2004;30(1):144–8.

[41] Jirásková N, Kadlecová J, Rozsíval P, Nekolová J, Pozlerova J, Dúbravská Z. Comparison of the effect of AquaLase and NeoSoniX phacoemulsification on the corneal endothelium. J Cataract Refract Surg 2008;34(3):377–82.

[42] Weaver Jr W, Timoshenko SP, Young DH. Vibration problems in engineering. John Wiley & Sons; 1990.

[43] Lallemand P, Luo L-S. Theory of the lattice Boltzmann method: dispersion, dissipation, isotropy, Galilean invariance, and stability. Phys Rev E 2000;61(6): 6546.

[44] Yu D, Mei R, Shyy W. A multi-block lattice Boltzmann method for viscous fluid flows. Int J Numer Methods Fluids 2002;39(2):99–120.

[45] Doyle JF. Nonlinear analysis of thin-walled structures: statics, dynamics, and stability. Springer Science & Business Media; 2013.

[46] Hsiao KM, Yang RT. A co-rotational formulation for nonlinear dynamic analysis of curved Euler beam. Comput Struct 1995;54(6):1091–7.

[47] Le T-N, Battini J-M, Hjiaj M. Efficient formulation for dynamics of corotational 2D beams. Comput Mech 2011;48:153–61.

[48] Kang SK. Immersed boundary methods in the lattice boltzmann equation for flow simulation. Texas A&M University; 2010. Doctor Thesis.

[49] Tan RK, Wang X, Perera SA, Girard MJ. Numerical stress analysis of the iris tissue induced by pupil expansion: comparison of commercial devices. PLoS ONE 2018; 13(3):e0194141.

[50] Doukas AG, McAuliffe DJ, Lee S, Venugopalan V, Flotte TJ. Physical factors involved in stress-wave-induced cell injury: the effect of stress gradient. Ultrasound Med Biol 1995;21(7):961–7.

[51] Alió JL, Fine IH. Minimizing incisions and maximizing outcomes in cataract surgery. Springer; 2010.

[52] Wang C, Tang H. Influence of complex driving motion on propulsion performance of a heaving flexible foil. Bioinspir Biomim 2018;14(1):016011.

[53] Wang C, Tang H. On the aeroelastic energy transfer from a Lamb dipole to a flexible cantilever. J Fluids Struct 2019;86:170–84.

[54] Wang CL, Tang H, Duan F, Yu SCM. Control of wakes and vortex-induced vibrations of a single circular cylinder using synthetic jets (in English) J Fluids Struct Jan 2016;60:160–79. https://doi.org/10.1016/j.jfluidstructs.2015.11.003. Article vol.

[55] Wang CL, Tang H, Yu SCM, Duan F. Active control of vortex-induced vibrations of a circular cylinder using windward-suction-leeward-blowing actuation (in English) Phys Fluids May 2016;28(5):14. https://doi.org/10.1063/1.4947246. Article volArt no. 053601.

[56] Wang CL, Tang H, Yu SCM, Duan F. Control of vortex-induced vibration using a pair of synthetic jets: influence of active lock-on (in English) Phys Fluids Aug 2017; 29(8):11. https://doi.org/10.1063/1.4996231. Article volArt no. 083602.

[57] Wang CL, Tang H, Yu SCM, Duan F. Lock-on of vortex shedding to a pair of synthetic jets with phase difference (in English) Phys Rev Fluids Oct 2017;2(10): 26. https://doi.org/10.1103/PhysRevFluids.2.104701. Article volArt no. 104701.

[58] Guo Z, Zheng C, Shi B. Discrete lattice effects on the forcing term in the lattice Boltzmann method. Phys Rev E 2002;65(4):046308.

[59] Luo L-S, Liao W, Chen X, Peng Y, Zhang W. Numerics of the lattice Boltzmann method: effects of collision models on the lattice Boltzmann simulations. Phys Rev E 2011;83(5):056710.

[60] He X, Luo L-S. Lattice Boltzmann model for the incompressible Navier–Stokes equation. J Stat Phys 1997;88:927–44.

[61] Hsiao KM, Yang RT. A co-rotational formulation for nonlinear dynamic analysis of curved euler beam. Comput Struct 1995;54(6):1091–7.

[62] Le T-N, Battini J-M, Hjiaj M. Efficient formulation for dynamics of corotational 2D beams. Comput Mech 2011;48(2):153–61.

[63] Paultre P. Dynamics of structures. John Wiley & Sons; 2013.

[64] Peskin CS. The immersed boundary method. Acta Numer 2002;11:479–517.

[65] Delouei AA, Nazari M, Kayhani M, Ahmadi G. Direct-forcing immersed boundary–non-Newtonian lattice Boltzmann method for transient non-isothermal sedimentation. J Aerosol Sci 2017;104:106–22.

[66] Karimnejad S, Delouei AA, Nazari M, Shahmardan M, Mohamad A. Sedimentation of elliptical particles using Immersed Boundary–Lattice Boltzmann Method: a complementary repulsive force model. J Mol Liq 2018;262:180–93.

[67] Karimnejad S, Delouei AA, Nazari M, Shahmardan M, Rashidi M, Wongwises S. Immersed boundary—Thermal lattice Boltzmann method for the moving simulation of non-isothermal elliptical particles. J Therm Anal Calorim 2019;138 (6):4003–17.

[68] Afra B, Delouei AA, Mostafavi M, Tarokh A. Fluid-structure interaction for the flexible filament's propulsion hanging in the free stream. J Mol Liq 2021;323: 114941.

[69] Cui J, Wang Z, Liu Y, Jin Y, Zhu Z. Three-dimensional simulation of lateral migration of fiber in a laminar channel flow. Int J Mech Sci 2022;236:107766.

[70] Jiang Q, et al. On the magnetic nanoparticle injection strategy for hyperthermia treatment. Int J Mech Sci 2022;235:107707.

[71] Ren F, Zhang F, Zhu Y, Wang Z, Zhao F. Enhancing heat transfer from a circular cylinder undergoing vortex induced vibration based on reinforcement learning. Appl Therm Eng 2024;236:121919.

[72] Wang Z, Zhao F, Fu Y, Deng F, Zeng L, Cui J. Towards energy harvesting through flow-induced snap-through oscillations. Int J Mech Sci 2023;254:108428.

[73] Wang Z, Zhao F, Xu B, Zeng L, Tang H. Effect of boundary conditions on energy harvesting of a flow-induced snapping sheet at low Reynolds number. Phys Fluids 2023;35(12). https://doi.org/10.1063/5.0171294.